Cold gas in distant galaxies

Boogaard, L.A.

6 | The average molecular gas content of star-forming galaxies at $z = 3 - 4$

Abstract

We study the molecular gas content of 24 star-forming galaxies at $z = 3 - 4$, with a median stellar mass of $10^{9.1}$ $M_\odot$, from the MUSE *Hubble* Ultra Deep Field (HUDF) Survey. Selected by their Lyα λ1216-emission and H_{F160W}-band magnitude, the galaxies show an average $\langle EW^0_{Ly\alpha} \rangle \approx 20$ Å, lower than typical Lyman Alpha Emitters, and a rest-frame UV spectrum more similar to Lyman Break Galaxies. We use rest-frame optical spectroscopy from KMOS and MOSFIRE, and the UV features observed with MUSE, to determine the systemic redshifts, which are offset from Lyα by $\langle \Delta v(Ly\alpha) \rangle = 346$ km s^{-1}, with a 100 to 600 km s^{-1} range. Stacking ^{12}CO $J = 4 \rightarrow 3$ and [C I] $^3P_1 \rightarrow {}^3P_0$ (and higher-J CO lines) from the ALMA Spectroscopic Survey of the HUDF (ASPECS), we determine 3σ upper limits on the line luminosities of 4.0×10^8 K km s^{-1}pc^2 and 5.6×10^8 K km s^{-1}pc^2, respectively (for a 300 km s^{-1} linewidth). Stacking the 1.2 mm dust continuum flux densities, we find a 3σ upper limit of 9 μJy. The inferred gas fractions, under the assumption of a 'Galactic' CO-to-H_2 conversion factor and gas-to-dust ratio, are in tension with previously determined scaling relations. This implies a substantially higher $\alpha_{CO} \geq 10$ and $\delta_{GDR} \geq 1200$, consistent with the sub-solar metallicity estimated for these galaxies ($12 + \log(O/H) \approx 7.8 \pm 0.2$). The low metallicity of $z \geq 3$ star-forming galaxies may thus make it very challenging to unveil their cold gas through CO or dust emission, warranting further exploration of alternative tracers, such as [C II].

L. A. Boogaard, R. J. Bouwens, D. Riechers, P. van der Werf, *et al.*
The Astrophysical Journal, submitted for publication

6.1 Introduction

The recent decade has witnessed a tremendous advance in the characterization of the cold molecular gas content of star forming galaxies at $z > 1$. Evidence is now mounting that the cold gas fraction of massive star-forming galaxies strongly increases up to at least $z \approx 3$ (e.g., Tacconi et al., 2010, 2013, 2018; Genzel et al., 2010, 2015; Geach et al., 2011; Dessauges-Zavadsky et al., 2015, 2020; Aravena et al., 2019, 2020). As the cold H_2 gas itself is radiatively dark, the molecular gas has to be traced by the emission from the ground-state rotational transition of Carbon Monoxide (^{12}CO, hereafter CO), or other tracers such as the emission from neutral atomic carbon ([C I]) or the long-wavelength dust continuum. Yet, observations of CO in (optically selected) star-forming galaxies at $z > 3$ remain challenging and have been limited to massive Lyman Break- or main sequence-selected galaxies and/or strongly lensed systems, with known redshifts (Baker et al., 2004; Coppin et al., 2007; Riechers et al., 2010; Magdis et al., 2012, 2017; Tan et al., 2013; Livermore et al., 2012; Saintonge et al., 2013; Dessauges-Zavadsky et al., 2015, 2017; Pavesi et al., 2019; Cassata et al., 2020), sometimes serendipitously detected and only identified as such *a posteriori* (Gowardhan et al., 2019).

The Atacama Large Millimeter Array Large Program ASPECS (The ALMA Spectroscopic Survey in the *Hubble* Ultra Deep Field (HUDF); Walter et al. 2016; Decarli et al. 2019) provides a unique opportunity to study the gas content of star forming galaxies at $z \geq 3$. ASPECS consists of spectral scans in ALMA Band 3 (85–115 GHz) and 6 (212–272 GHz), probing molecular gas and dust in galaxies without any target preselection. These data unveil emission from CO, [C I] and dust-continuum in several star-forming galaxies at $z = 1 - 4$ (González-López et al., 2019, 2020; Boogaard et al., 2019, 2020), providing key constraints on the empirical scaling relations describing the evolution of the gas and dust content in galaxies (Aravena et al., 2019, 2020), the evolution of the cosmic molecular gas density (Decarli et al., 2019, 2020) and the baryon cycle (Walter et al., 2020).

Key to the exploration of the ASPECS data are the large number of spectroscopic redshifts provided by the Multi Unit Spectroscopic Explorer (MUSE) HUDF Survey (Bacon et al., 2017). Through its unparalleled sensitivity for faint emission lines, MUSE has detected many galaxies at $z \geq 3$, where the bright H I Lyα λ1216 line enters the integral-field spectrograph ($4750 - 9300$Å; $\lambda/\Delta\lambda \approx 3000$; Inami et al. 2017), probing the faint end of the Lyα luminosity function down to below 0.1 $L^*_{\rm Lya}$ (Drake et al., 2017).

Exploiting the large number of redshifts from MUSE, we can push the gas mass-sensitivity of ASPECS at $z \geq 3$ to its limits through stacking (in particular, CO $J = 4 \rightarrow 3$ becomes accessible at $z \geq 3.0115$). Indeed, Inami et al. (2020) have shown that at lower redshifts, $z = 1 - 2$, we can recover CO emission below the formal sensitivity threshold of ASPECS, by stacking on the accurate systemic redshifts from MUSE.

However, the MUSE redshifts at $z \geq 3$ obtained from Lyα cannot be used for stacking. Because Lyα is a resonant transition, the photons are easily scattered by the neutral gas in- and surrounding a galaxy, shifting the peak of the emission away from the systemic velocity by several hundred km s^{-1} (e.g., Shapley et al., 2003; Verhamme et al., 2018; Muzahid et al., 2020). This means that the line emission tracing the molecular gas could be completely washed out by the noise if non-systemic Lyα-redshifts are used for stacking.

Fortunately, because we have approximate redshifts from Lyα, these targets can be effectively followed-up simultaneously with multi-object, near-infrared spectrographs, such as the K-band Multi Object Spectrograph (KMOS) at the Very Large Telescope and the Multi-Object Spectrometer For Infra-Red Exploration (MOSFIRE) at the Keck Observatory. These data can constrain the systemic redshift by targeting the rest-frame optical lines such as Hβ λ4863 and [O III] $\lambda\lambda$4960, 5008 in the K-band (out to $z = 3.812$).

In this paper, we constrain the molecular gas content of star-forming galaxies at $3.0115 < z < 3.812$, by stacking their molecular gas signal through the outlined three step process. We 1) identify the galaxies from MUSE and 2) determine their systemic redshifts through rest-frame NIR spectroscopy with KMOS/MOSFIRE (as well as rest-UV features from MUSE; § 6.2). We then 3) turn to ALMA to stack the CO and [C I] signal from the ASPECS data, as well as the 1.2 mm dust continuum (§ 6.3). We do not detect any (line) emission in the stacks (at the 3σ level) and discuss the implications of this non-detection on metallicity, the CO-to-H_2 conversion factor ($\alpha_{\rm CO}$) and gas-to-dust ratio ($\delta_{\rm GDR}$) in § 6.4. The results highlight that the metallicity evolution of star-forming galaxies makes it increasingly challenging to infer the molecular gas content at higher redshifts, which warrants the further theoretical and observational exploration of alternative tracers, in particular the [C II] λ158 μm line.

Throughout this paper, we report wavelengths in vacuo and magnitudes in the AB system (Oke & Gunn, 1983), and adopt a Chabrier (2003) initial mass function. We use log to denote $\log_{10}$ and ln for the natural logarithm. We adopt a concordance cosmology with $H_0 = 70\,{\rm km\,s^{-1}\,Mpc^{-1}}$, $\Omega_m = 0.3$ and $\Omega_\Lambda = 0.7$, in good agreement with the measurements from Planck Collaboration et al. (2016).

6.2 Observations and sample selection

6.2.1 Parent sample selection and physical properties

We construct a parent sample of galaxies from the MUSE HUDF Survey Data Release 2 catalog,[42] which is an updated and revised version of the DR1 catalog (Bacon et al., 2017; Inami et al., 2017). In short, the catalog contains both emission line-selected sources (from ORIGIN; Mary et al., 2020) and continuum-selected sources (from the *Hubble Space Telescope* (*HST*) catalog by Rafelski et al. 2015) for which the redshifts are determined automatically. These sources have subsequently been verified by several independent groups of experts that inspect the redshift, the multiwavelength counterpart associations, and assign a confidence flag (ZCONF; where confidence ≥ 2 implies a secure redshift, determined by at least two spectral features). Specifically, we use the following criteria:

- Select all objects with $3.0115 < z < 3.812$ and ZCONF ≥ 2, that have a *HST* counterpart in the Rafelski et al. (2015) catalog.
- Restrict to objects that lie within the 4.55 arcmin^2 region of the ASPECS Band 3 mosaic where the sensitivity is $\geq$ 40% of the primary beam peak sensitivity at 99.5 GHz.

[42] DR2 v0.1; R. Bacon, *et al.*, in prep.

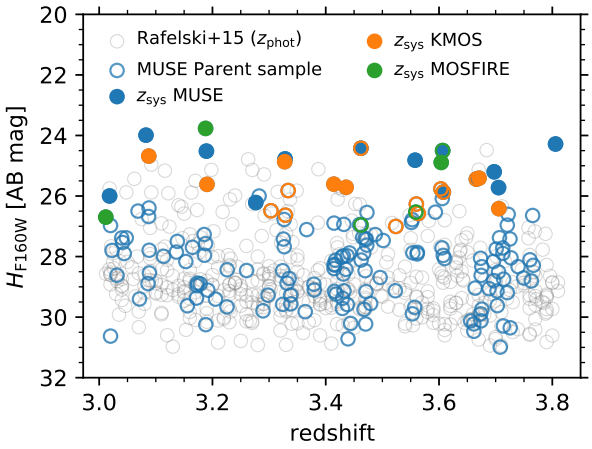

Figure 6.1: The H_{F160W}-band magnitude of the galaxies considered in this paper as a function of redshift. The open circles show the parent sample of all galaxies with $3.0115 \leq z < 3.812$ within the ASPECS field ($\geq$ 40% of the primary beam peak sensitivity) that have a MUSE redshift (from Lyα λ1216) in blue, while the gray circles show all galaxies in the same field with a photometric redshift (Rafelski et al., 2015). Galaxies targeted for KMOS or MOSFIRE follow-up are shown in orange and green, respectively. The filled circles show galaxies for which we obtained a systemic redshift measurement from MUSE (blue), KMOS (orange) or MOSFIRE (green).

- Remove three X-ray detected sources that are classified as having an active galactic nucleus (AGN; MUSE-1051, MUSE-1056 and MUSE-6672), based on the *Chandra* 7 MS data (Luo et al., 2017).

There are a total of 168 galaxies in the parent sample constructed this way. The H_{F160W} magnitude of the parent sample is shown as a function of redshift in Figure 6.1. Because of the sensitivity of MUSE to faint emission line sources, it consists almost exclusively of galaxies that are selected by their Lyα λ1216-emission. Only six galaxies are not marked as such: one is MUSE-50, which does show double peaked Lyα-emission on top of strong Lyα-absorption, as well as strong UV lines. The other five indeed show little Lyα-emission: one is a faint C IV $\lambda\lambda$1548, 1551-only-emitter, while the other four have bright enough UV continuum to have their systemic redshifts determined from absorption lines (see § 6.2.2).

Because the Lyα emission may peak in the halo of a galaxy, the association of a MUSE source with an *HST* counterpart can be ambiguous and is typically resolved on during the redshift determination process. The associations adopted here are listed in Table 6.2 and are in all cases supported by a second tracer of the systemic redshift. In the case of MUSE-6518, the photometry is completely blended with a $z = 0.83$ foreground object and we do not use it to obtain physical properties.

We determine a stellar mass (M_*) and star-formation rate (SFR) for all galaxies in the parent sample by fitting eleven bands of *HST* (Rafelski et al., 2015) and four bands of *Spitzer*/IRAC photometry, using the high-z extension of the spectral energy distribution fitting code MAG-

PHYS (Da Cunha et al., 2008, 2015). As in Labbé et al. (2006, 2010, 2015), the deblended *Spitzer*/IRAC photometry was measured with MOPHONGO, using the *HST* observations as a template, in the deep $\sim$ 200-hour data from the GREATS program (M. Stefanon, et al., in prep.). The latter provides constraints on the rest-frame optical part of the spectral energy distribution redward of the 4000-Å break and is critical to pin down the stellar masses of our galaxies. The results are listed in Table 6.2, for the galaxies in the systemic redshift sample.

As part of the DR2, the spectra of all galaxies are modeled with PYPLATEFIT (R. Bacon, *et al.*, in prep.), the Python implementation of the spectrum fitting code PLATEFIT, originally developed for the *Sloan Digital Sky Survey* (Tremonti et al., 2004; Brinchmann et al., 2004, 2008). The most salient features of PYPLATEFIT, relevant to this work, are that it can simultaneously model both the emission- and absorption lines, as well as the stellar continuum, allowing for velocity differences between groups of lines (such as Lyα and other UV lines). All lines are modeled using Gaussians except Lyα, for which a (double) asymmetric Gaussian[43] is used (double if the Lyα line is double-peaked).

6.2.2 Measurement of systemic redshifts

We obtain systemic redshifts for galaxies in our parent sample from either the rest-frame UV features using MUSE or the rest-frame optical emission lines with near-IR spectroscopy. For the near-IR follow-up, targets were selected by their H_{F160W} magnitude (as a proxy for stellar mass) and the absence of a systemic redshift from MUSE in the DR1 reductions. Fainter targets were sometimes observed because brighter targets were no longer accessible given the small size of the HUDF and physical limitations in the positioning arms and slits of multi-object spectrographs.

MUSE

For a subset of galaxies we can determine the systemic redshift directly from the MUSE spectra, using the weaker rest-frame UV emission lines, or absorption features. We identify objects in the parent sample that are cataloged as having S/N $>$ 3 in at least one UV emission line. We focus specifically on O III] $\lambda\lambda$1661, 1666 S III] $\lambda\lambda$1883, 1892, C III] $\lambda\lambda$1907, 1909 and a selection of absorption lines,[44] that trace the systemic redshift. We also fit narrow He II λ1640 together with the emission lines, finding it at a similar velocity offset as the other UV lines. We do not use the resonant lines, such as C IV $\lambda\lambda$1548, 1551, which can be offset from the systemic velocity like Lyα. To identify absorption line redshifts, we inspect all objects with $V_{\mathrm{F606W}} \leq 27$ and/or $i_{\mathrm{F775W}} \leq 27$, finding that we can determine these in several galaxies down to $i_{\mathrm{F775W}} = 26$. We use PYPLATEFIT to fit the selected spectra, performing 200 bootstrap iterations to obtain a more robust estimate of the uncertainties (both on Lyα and the other features). We only keep the objects that remain at S/N $>$ 3.5 in at least one emission line or

[43] Also known as the Skew normal distribution, $f(x) = 2\phi(x)\Phi(\gamma x)$, where $\phi(x)$ is the standard normal (Gaussian) distribution, $\Phi(x)$ is the cumulative distribution function for a standard normal distribution, and γ is the skewness parameter.

[44] Si II λ1260, O II λ1302, Si II λ1304, C II λ1335, Si IV $\lambda\lambda$1394, 1403, Fe II $\lambda\lambda$1608, 1611, Al II λ1671 and Al II $\lambda\lambda$1854, 1862.

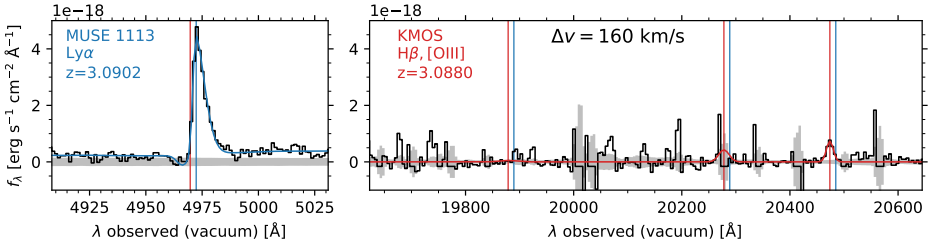

Figure 6.2: Rest-frame ultraviolet and optical spectra for the first galaxy in the sample with near-infrared follow-up. The *left* panel shows the MUSE spectrum surrounding the Lyα line. The *right* panel shows the continuum subtracted KMOS spectrum around the Hβ λ4863 and [O III] $\lambda\lambda$4960, 5008 lines. In both panels the vertical blue and red lines indicate the redshift of Lyα and the systemic redshift, respectively, determined from the fit to the spectrum (shown in the same color). This particular galaxy is detected in Lyα λ1216 and [O III] λ5008, but not in Hβ λ4863, showing a positive velocity offset between the red peak of Lyα and the systemic redshift (note [O III] λ4960 falls on top of a skyline). Spectra of the remaining galaxies with KMOS or MOSFIRE observations are shown in Figure 6.12 in § 6.B.

the sum of the absorption features. In addition, we keep MUSE-1360 as a tentative candidate, having both a tentative detection in the KMOS data and an absorption line redshift at S/N = 3. The $z_{\rm Lyff}^{\rm red}$ and $z_{\rm sys}$, with their bootstrapped uncertainties, are provided in Table 6.2 (where $z_{\rm Lyff}^{\rm red}$ is the redshift of the red peak of Lyα). We note that three of these sources were also part of the study of Lyα-velocity offsets by Verhamme et al. (2018).

In principle, one could estimate the systemic redshift by using half of the peak separation for Lyα-lines with a blue bump (Verhamme et al., 2018). Indeed, a few galaxies in our sample also show blue bump-emission. However, systematic searches for blue-bump Lyα-emitters are still on-going and we therefore do not include such a sample at this stage. Furthermore, the presence of a blue bump requires specific radiative transfer conditions and selecting a sample in such a way may introduce a bias in the stack.

KMOS

The KMOS observations were taken in two ESO periods, as part of 099.A-0858(A) (PI: Bouwens) and 0101.A-0725(A) (PI: Boogaard). We used the HK grating (with a spectral resolution of $\lambda/\Delta\lambda \approx 1800$) in 5 Observing Blocks (OBs) per period, with an ABA ABA AB sky-offset pattern between the science (A) and sky (B) frames with 300 s integrations and 0.″2 dithering offsets. In total we targeted 17 galaxies, with (final) on source times ranging between 200 and 250 minutes. We also included a bright quasar on all masks to control the astrometry, from which we measure the image quality to be around 0.″75 and 0.″85 in the reduced P99 and P101 data, respectively.

We reduce the data using the ESO KMOS pipeline version 2.1.0 (Davies et al., 2013), using the standard star observations for the zeropoint, response and telluric correction. We enable the `background` flag to correct for differences in the residual background level between the exposures by applying a constant offset, estimated by taking the mode of the pixel values

after excluding the brightest 25%. We discard the data from one detector for the second A frame of the first OB in period 99, which shows a strong background offset. We experimented with further reducing the sky line residuals using the `sky-tweak` and `molecfit` options of the pipeline, but found that these sometimes introduces artifacts in the data. As our lines were selected to be away from the sky lines as much as possible, we therefore do not apply these corrections. Because of the density of the skylines around [O II] λ3727 in the H-band, we focus on the Hβ λ4863 and [O III] $\lambda\lambda$4960, 5008 in the K-band. We apply radial velocity corrections[45] to shift every reduced A-B frame to the solar system barycentric frame (the mean $\langle v_r \rangle = 17.3$ km s^{-1}).

We correct for positional shifts between the different OBs by centering on the continuum position of the reference quasar, which we model with a 2D Gaussian. As objects were placed on different IFUs between periods, their position relative to the reference quasar change. We therefore first combine and analyze the data from each period separately. To identify the spatial position of each (emission line-only) object on its IFU in each period, we (i) extract spectra at the a-priori expected position (that is, the quasar position or the center of the cube) using the 2D fit of the reference quasar as a spatial model, (ii) identify the brightest spectral line, [O III] λ5008, based on the Lyα redshift and determine its central wavelength and line width using a Gaussian fit, (iii) collapse the cube over the channels with line emission to make a 'narrow band', through multiplication with the Gaussian fit along the wavelength axis, and (iv) identify the spatial position in the narrow band image. We iterate steps (i)-(iv) until we converge on spatial position. Finally, we combine the data from both periods using the best positions and repeat the same steps to obtain the final spectra.

We conservatively only consider the objects for which we can identify the line(s) in each half of the data separately, which gives strong confidence that the line(s) are not (caused by) sky line residuals. We exclude one source where the blueshift of the lines relative to Lyα resulted in them being too close to the skylines to determine the centroid and four more sources where a tentative feature was only seen in one period. In total, we confidently detect the rest-frame optical line(s) in 7/17 galaxies. As an example, we show the MUSE and KMOS spectrum for one of the galaxies in Figure 6.2. The spectra of the remaining galaxies are shown in Figure 6.12 in § 6.B.

Finally, we determine the redshift by simultaneously fitting Gaussians (in vacuo) to the Hβ λ4863 and [O III] $\lambda\lambda$4960, 5008 lines (using LMFIT; Newville et al. 2019b). We use the inverse of the error spectrum as weights and subtract a running median continuum from the spectrum prior to the fitting. The resulting redshifts are reported in Table 6.2.

MOSFIRE

The MOSFIRE observations were taken in the night of 28 November 2018 as part of program 2018B_N182 (PI: Riechers). We observed a single K band mask with 0.″7 slits ($\lambda/\Delta\lambda \approx$ 3610). We used an AB dither pattern with 180 second exposures, totaling to 108 minutes of exposure time on source, with an average seeing of 0.″7. The data were reduced using the

[45] $\lambda' = \lambda\sqrt{(1 + v_r/c)/(1 - v_r/c)}$, where λ' and λ are the corrected and uncorrected wavelengths, respectively, c is the speed of light and v_r is the radial velocity correction to the solar system barycenter, computed with `astropy.coordinates.SkyCoord.radial_velocity_correction`.

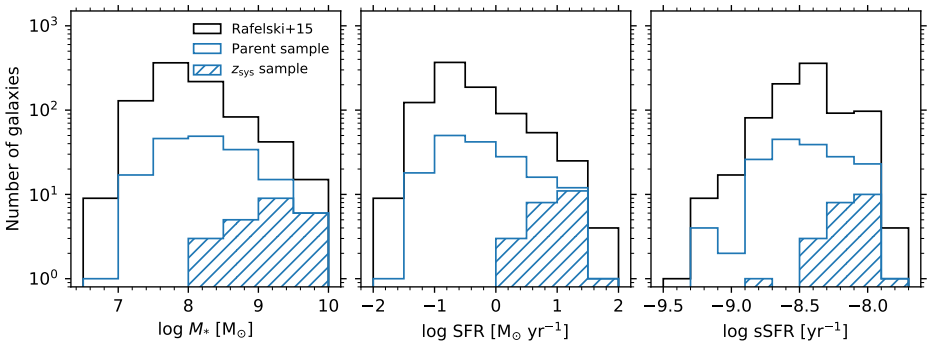

Figure 6.3: Histograms of the stellar mass (M_*), star formation rate (SFR) and specific SFR (sSFR = SFR/M_*) of the galaxies for which we determine a systemic redshift ($z_{\rm sys}$), compared to the parent sample from MUSE at $3.0115 \leq z < 3.812$ and all galaxies from the photometric redshift catalog by Rafelski et al. (2015).

standard MOSFIRE Data Reduction Pipeline (Release 2018),[46] using the Neon arc lamps for the wavelength calibration. As our objects generally do not show any continuum, we first manually identify (candidate) emission lines in the rectified, two dimensional spectra (based on the Lyα redshift). We then optimally extract the one dimensional spectra using a Gaussian model for the spatial profile. As all data were taken on a single night, we apply the radial velocity correction to the final spectra ($v_r = -9.2\,{\rm km\,s^{-1}}$).[47]

In total, we detect the rest-frame optical lines in 4/7 of the galaxies on the mask that are part of our parent sample (including MUSE-6518, with blended *HST* photometry). Their spectra are shown in Figure 6.12. We measure the redshifts as described in § 6.2.2 and report the results in Table 6.2.

6.2.3 Final systemic redshift sample

In total, we use MUSE, KMOS and MOSFIRE to obtain systemic redshifts for 24 galaxies, 20 of which are originally identified by their Lyα-emission, with an average redshift of $\langle z \rangle = 3.45$. The $H_{\rm F160W}$ magnitude of the final sample is shown in comparison to the MUSE parent sample in Figure 6.1. We have a systemic redshift for most galaxies in the parent sample down to $H_{\rm F160W} = 26$. Because the parent sample is Lyα-selected, this raises the question how representative our sample is for the broader population of galaxies at these epochs. We therefore compare our (parent) sample to all galaxies at the same redshift and over the same field, from the photometric redshift catalog by (Rafelski et al., 2015, updated with the MUSE redshifts), after excluding the X-ray AGN (Luo et al., 2017, as we did for the parent sample), see Figure 6.1.

We show a histogram of the physical properties of the galaxies in Figure 6.3. The median

[46] https://github.com/Keck-DataReductionPipelines/MosfireDRP
[47] See footnote 45

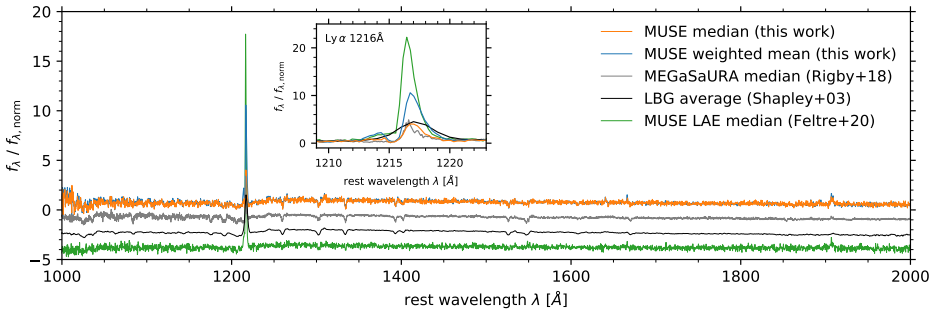

Figure 6.4: Composite MUSE spectrum of the sample, from both weighted mean (blue) and median (orange) stacking (at 0.3 Å resolution) using the systemic (non-Lyα) redshifts. We compare to the average Lyman Break Galaxy (LBG) spectrum at $z \sim 3$ (black) from (Shapley et al., 2003, 1 Å resolution), the composite spectrum of 14 strongly lensed, star-forming galaxies at $1.6 < z < 3.6$ from the MEGASAURA sample (Rigby et al. 2018; the pivot normalized, median stack at 0.1 Å resolution) and the composite MUSE spectrum of all 220 LAEs at $2.9 < z < 4.6$ (Feltre et al., 2020, median stack; note their weighted mean stack is very similar, with slightly stronger Lyα emission). We normalize all spectra to the median flux density at 1267–1276 Å and offset the literature spectra by −1.5, −3, and −4.5 for clarity. The inset shows a zoom-in of the Lyα-line without vertical offsets. Overall, the composite MUSE spectrum is very similar to the LBGs and MEGASAURA, showing comparable UV continuum and absorption features, slightly stronger UV emission lines, and a comparable strength of the Lyα-line in the median spectrum (notably showing a blue bump). In contrast, the median stack of all LAEs from Feltre et al. (2020) shows significantly stronger Lyα-emission, even when compared to the weighted mean spectrum of our galaxies.

stellar mass and SFR of the sample is $10^{9.1}$ M$_\odot$ and 10 M$_\odot$ yr^{-1}. The sample encompasses $\geq$ 50% of the galaxies in the MUSE parent sample in the bins down to $M_* \geq 10^9$ M$_\odot$ and SFR ≥ 3 M$_\odot$ yr^{-1}, and $\geq$ 20% of the galaxies in the broader photometric catalog, down to the same limits.

Our galaxies are faint Lyα-emitters in comparison to narrow band-selected samples. The typical Lyα luminosity of our sample is $L_{\mathrm{Ly}\alpha} = 10^{42}$ erg s^{-1} $\approx 0.2\, L^*_{\mathrm{Ly}\alpha}$ at $z = 3.5$ (e.g., Ouchi et al., 2008; Drake et al., 2017; Herenz et al., 2019). The average rest-frame equivalent-width[48] $\langle \mathrm{EW}^0_{\mathrm{Ly}\alpha} \rangle \approx 20$ Å of our sample is also small, especially when considering that ≈ 25 Å is the typical lower limit for the definition of a (narrow band-selected) Lyα-emitter (or LAE). This is likely due to our selection towards objects that are bright in H_{F160W}. As such, our galaxies are not necessarily comparable to the typical sample of LAEs, but arguably more similar to the average population of (low-mass) star-forming galaxies

To illustrate this point, we stack the MUSE spectrum of all the galaxies in our sample, using the systemic redshifts, following Feltre et al. (2020). We perform a median and weighted mean stack, after normalizing each of the spectra by the median flux density at $1267 - 1276$ Å (matching Rigby et al. 2018). The result is shown in Figure 6.4. We compare the composite

[48]The rest-frame equivalent width is computed by PYPLATEFIT, from the total flux in Lyα (including a possible blue bump) over the modeled continuum flux density at 1216Å (defined such that a positive value indicates emission).

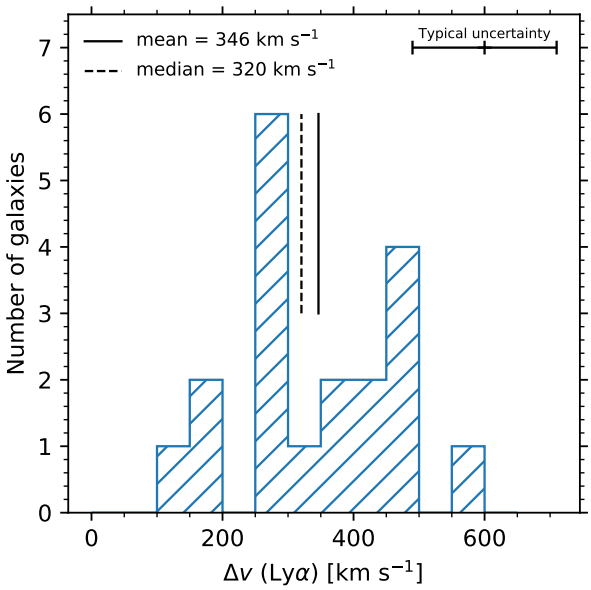

Figure 6.5: Histogram of the velocity offset of Lyα λ1216 with respect to the systemic redshift, Δv(Lyα). The vertical lines indicate the mean and median velocity offset in the sample. The typical $\pm 1\sigma$-uncertainty on the velocity offset is indicated in the top right.

MUSE spectrum to the average spectrum of $z \sim 3$ Lyman Break Galaxies (LBGs; Shapley et al., 2003), the composite spectrum of 14 strongly lensed, star-forming galaxies at $1.6 < z < 3.6$ from the MegaSaura sample (Rigby et al., 2018) and the composite MUSE spectrum of all 220 LAEs at $2.9 < z < 4.6$ from Feltre et al. (2020). Overall, the similarities in the literature spectra of LBGs and star-forming galaxies and the (median) composite spectrum of our sample, with significantly weaker Lyα-emission than the average LAE spectrum, support the case that our galaxies are more similar to the population of star-forming galaxies at these epochs.

6.3 Results

6.3.1 Velocity offsets

We plot the velocity offset of Lyα λ1216 with respect to the systemic redshift in Figure 6.5, defined as $\Delta v(\mathrm{Ly}\alpha) = c(z^{\mathrm{red}}_{\mathrm{Lyff}} - z_{\mathrm{sys}})/(1 + z_{\mathrm{sys}})$, where c is the speed of light. Our galaxies show a mean velocity offset of $\langle \Delta v(\mathrm{Ly}\alpha) \rangle = 346\,\mathrm{km\,s^{-1}}$, with a range from 100 to 600 km s^{-1}.

For comparison, the mean $\Delta v(\mathrm{Ly}\alpha) \approx 200 - 250\,\mathrm{km\,s^{-1}}$ in the LAE samples at $z = 2 - 3$ (Erb et al., 2014; Trainor et al., 2015), while the $z \sim 3$ LBG sample from Shapley et al. (2003)

Table 6.1: Lines stacked in this paper.

Transition	ν_0 (GHz)	$z_{\rm min}$	Band	N	$S_\nu\Delta v$ (mJy km s^{-1})	$S_\nu\Delta v$ (mJy km s^{-1})	L' (K km s^{-1} pc^2)
(1)	(2)	(3)	(4)	(5)	(6)	(7)	(8)
Systemic redshift sample (Figure 6.6)							
CO $J = 4 \rightarrow 3$	461.04	3.0115	3	23	-3.2 ± 4.2	<12.7	$<4.0 \times 10^8$
[C I] $^3P_1 \rightarrow {}^3P_0$	492.16	3.2823	3	16	4.9 ± 6.8	<20.5	$<5.6 \times 10^8$
CO $J = 9 \rightarrow 8$	1036.91	2.8122	6	23	33.3 ± 12.7	<38.1	$<2.3 \times 10^8$
CO $J = 10 \rightarrow 9$	1151.99	3.2352	6	16	7.4 ± 16.6	<49.8	$<2.5 \times 10^8$
Lyα-selected galaxies only							
CO $J = 4 \rightarrow 3$	461.04	3.0115	3	18	-7.3 ± 5.0	<15.0	$<4.7 \times 10^8$
[C I] $^3P_1 \rightarrow {}^3P_0$	492.16	3.2823	3	12	11.0 ± 7.9	<23.8	$<6.5 \times 10^8$
CO $J = 9 \rightarrow 8$	1036.91	2.8122	6	19	39.5 ± 14.0	<42.2	$<2.6 \times 10^8$
CO $J = 10 \rightarrow 9$	1151.99	3.2352	6	13	16.2 ± 18.8	<56.5	$<2.8 \times 10^8$

Notes. $\langle z \rangle = 3.45$, $\Delta v = 300$ km s^{-1}. (1) Stacked transition (2) Rest frequency (3) Minimum redshift at which the transition is covered by ASPECS. (4) Band that contains transition. (5) Number of objects in stack. (6) Line flux in stack. (7) 3σ upper limit on line flux. (8) 3σ upper limit on line luminosity.

shows a greater mean velocity offset of 650 km s^{-1}. The relatively large velocity offsets imply a larger H I column density and lower Lyα escape fraction, consistent with the low $\mathrm{EW}^0_{\mathrm{Ly}\alpha}$ of our galaxies (Shapley et al., 2003; Erb et al., 2014; Yang et al., 2017b).

The broad distribution in Figure 6.5 also reflects the smoothing function by which the stacking signal would be diluted if $z^{\rm red}_{\rm Lyff}$ would be used for stacking, in particular because the ALMA data has a higher velocity resolution. This highlights the need for systemic redshifts.

6.3.2 ALMA Stacking

With the systemic redshifts in hand, we turn to the ALMA data. We use the ASPECS Band 3 (González-López et al., 2019; Decarli et al., 2019) and Band 6 (González-López et al., 2020; Decarli et al., 2020) datacubes at their native resolution ($\approx$ 20 km s^{-1} in both cases). The root-mean-square (rms) error spectra reach ≈ 0.2 and 0.5 mJy beam^{-1} channel^{-1} in Band 3 and Band 6, respectively (at the center of the field, varying with frequency).

Before extracting the spectra, we first shift the ALMA cubes from the Kinematic Local Standard of Rest (LSRK) to the Barycentric frame, using the CASA task `imreframe` ($\Delta v = -16.78$ km s^{-1}), such that all our spectroscopic data are on the same velocity frame. We then extract pixel spectra at the *HST* positions (Rafelski et al., 2015) of our galaxies, after correcting for the known astrometric offset ($\Delta\alpha = 0\farcs076$, $\Delta\delta = -0\farcs279$; Dunlop et al. 2017, consistent with Franco et al. 2020). These spectra should contain all the flux as our sources are expected to be unresolved by the ASPECS synthesised beam ($1\farcs8 \times 1\farcs5$ in Band 3 and $1\farcs5 \times 1\farcs1$ in Band 6). Their spatial extent in the rest-frame UV is significantly smaller, with a median effective radius in $H_{\rm F160W}$ of $\approx 0\farcs2$ (van der Wel et al., 2012).

Inspecting the spectra around the systemic redshift, none of the galaxies are individually detected in their CO or [C I] emission lines at the 3σ level. We therefore stack the spectra

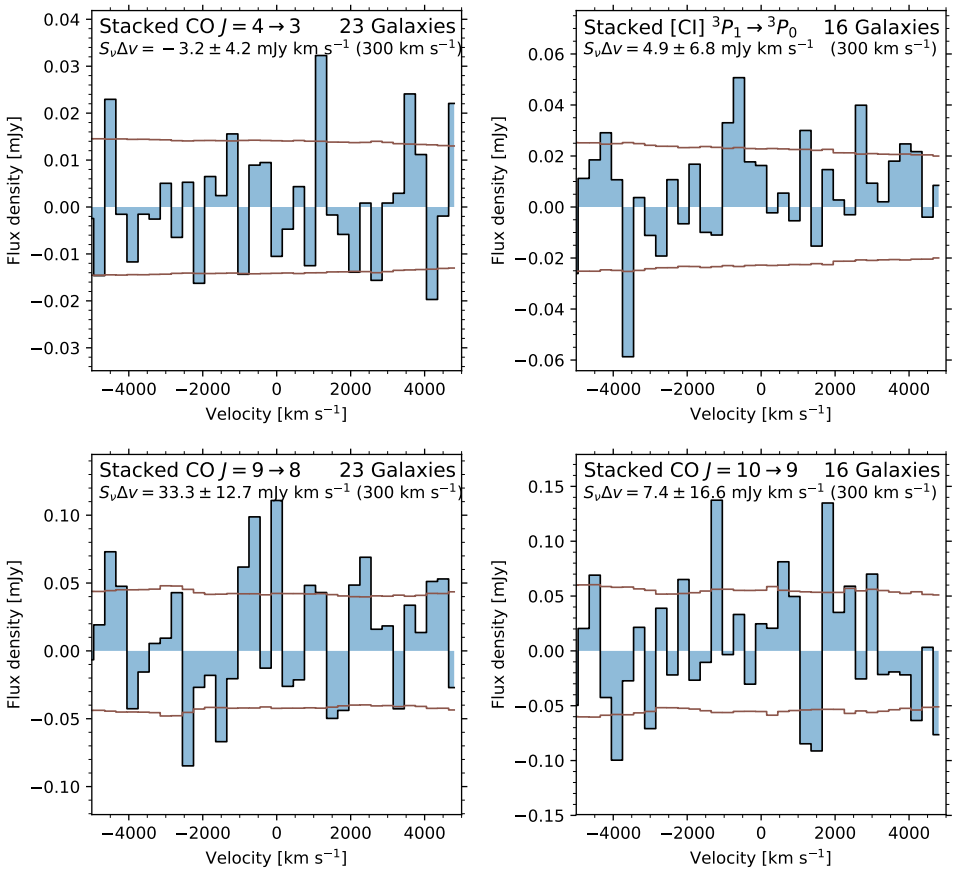

Figure 6.6: Stacked spectra of the ^{12}CO and [C I] transitions of the full sample. The spectrum is shown in blue and the brown line shows the root-mean-square noise (propagated through the $1/\sigma^2$-weighting of the stack). The stacked transition, the number of galaxies in the stack, the integrated line flux in the zero-velocity channel and the channel width (300 km s^{-1}) are indicated in each panel. We do not detect any emission in any of the transitions and provide 3σ upper limits in Table 6.1.

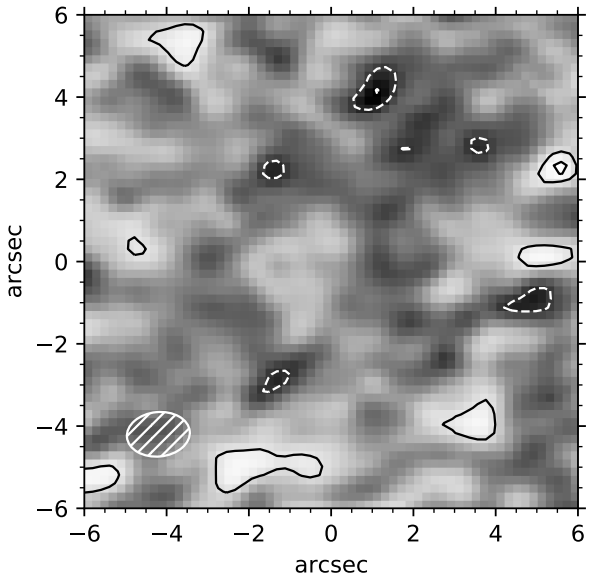

Figure 6.7: Stack of the 1.2 mm dust continuum. The cutout size is $12'' \times 12''$ and the synthesised beam is indicated in the bottom left corner. Contours are drawn starting at $\pm 2\sigma$ in steps of $\pm 1\sigma$ (dashed contours indicate negative signal). No emission is detected at the 3σ level, implying an upper limit of $9\,\mu$Jy.

as follows (Boogaard et al., 2020, cf. Spilker et al. 2014). We first create a grid in velocity space, centered around zero, with 300 km s^{-1} wide channels. The channel width was chosen based on the mean rest-frame UV/optical line-width ($\approx$ 200 km s^{-1}), such that $>$ 90% of the stacked line flux is expected to fall within the single central channel. We convert each observed spectrum to velocity space, centered around the line, and bin it onto the velocity grid. We then stack the spectra by taking the $1/\sigma^2$-weighted mean in each velocity channel (where σ is the error) and determine the uncertainty by propagating the error spectrum in the same manner. We finally measure the flux density and the corresponding uncertainty in the zero-velocity channel.

The stacked spectra are shown in Figure 6.6. None of the lines are detected in the stack at a signal-to-noise ratio greater than three. The stack of CO $J = 9 \rightarrow 8$ shows some signal at the $2 - 3\sigma$ level, but we do not consider this a detection. We compute 3σ upper limits on the integrated line flux, $S_\nu \Delta v$, from the uncertainty in the zero-velocity channel of the stacked spectrum (at 300 km s^{-1} resolution). We determine the corresponding upper limits on the line luminosities via

$$L' = 3.255 \times 10^7 \, S_\nu \Delta v \, d_L^2 \, \nu_{\rm obs}^{-2} (1+z)^{-3} \, {\rm K\,km\,s^{-1}\,pc^2} \tag{6.1}$$

(Solomon et al., 1992b; Carilli & Walter, 2013), adopting the luminosity distance (d_L) and observed frequency ($\nu_{\rm obs}$) at the average redshift of the sample, $z = 3.45$. The results can be

found in Table 6.1. We also perform additional stacks, including only the galaxies with the highest stellar masses ($M_* \geq 10^{9.0}$, $\geq 10^{9.5}$ and $\geq 10^{10}$ $M_\odot$) and the highest star formation rates (SFR ≥ 3.2 and $\geq 10\,M_\odot\,yr^{-1}$), but do not obtain any detections.

None of the galaxies are individually detected at the 3σ level in the deep 1.2 mm dust continuum map (González-López et al., 2020; Aravena et al., 2020). In addition to the line stack, we therefore also perform a weighted mean stack of the 1.2 mm dust continuum data for the full sample (following the approach from J. Bouwens et al., 2016; Bouwens et al., 2020, again applying the astrometric offset). We do not obtain a detection, measuring a flux of $S_\nu = 1 \pm 3\,\mu$Jy (Figure 6.7), implying an upper limit of $\leq 9\,\mu$Jy (3σ).

6.4 Discussion

6.4.1 Molecular gas masses

Stacking the $\langle z \rangle = 3.45$ star-forming galaxies in the HUDF by their systemic redshifts, we find that $L'_{\mathrm{CO}\ J=4\rightarrow3} \leq 4.7 \times 10^8\,\mathrm{K\,km\,s^{-1}\,pc^2}$. This result puts an upper limit on the molecular gas mass via

$$M_{\mathrm{mol}} = \alpha_{\mathrm{CO}} r_{J1}^{-1} L'_{\mathrm{CO}\ J\rightarrow J-1}, \tag{6.2}$$

where α_{CO} is known as the CO-to-H_2 conversion factor (a light-to-mass ratio) and r_{J1} is the excitation correction, needed to convert the observed CO luminosity to $L'_{\mathrm{CO}\ J=1\rightarrow0}$. There is no direct measurement of the CO excitation in the galaxies under consideration. Valentino et al. (2020a) measured an average $r_{41} = 0.36 \pm 0.06$ in their sample of star-forming galaxies at $z = 1.25$, while Tacconi et al. (2018) assume an average $r_{41} = 0.42$, constant with redshift. Boogaard et al. (2020), however, have shown that there is significant evolution in the CO excitation of gas mass-selected samples, with the average r_{41} increasing from 0.3 up to 0.6 between $z = 1{-}2$ and $z = 2{-}3$. Indeed, Dessauges-Zavadsky et al. (2017) find $r_{41} = 0.60{\pm}0.17$ in the strongly lensed MACSJ0032-arc at $z = 3.6$, with a similar $M_* \approx 10^{9.7}$ $M_\odot$ as our sample average (though significantly higher SFR $\approx 50\,M_\odot\,yr^{-1}$). If the excitation scales with SFR surface density (Daddi et al., 2015; Valentino et al., 2020a; Boogaard et al., 2020), this may suggest the excitation to be lower in our galaxies on average. We therefore loosely assume that $r_{41} = 0.5 \pm 0.2$, broadly encompassing the literature values. Note that higher excitation implies a smaller gas mass (Equation 6.2). As we are dealing with an upper limit on the gas mass in the first place, we effectively assume a lower limit on the excitation of $r_{41} \geq 0.3$, in good agreement with observations.

A major uncertainty in the molecular gas estimate comes from α_{CO}. For star forming galaxies at high redshift 'Galactic' conversion factors are typically assumed, consistent with observations in massive star forming galaxies (Daddi et al., 2010a). However, the value of α_{CO} has been observed to increase strongly at low metallicity (Z; Maloney & Black 1988; Israel 1997), where the decreased shielding leads to dissociation of CO deeper into the clouds (e.g., Wolfire et al. 2010, see Bolatto et al. 2013 for a review). Several calibrations for the metallicity dependence of the CO-to-H_2 conversion factor exist in the literature, both determined empirically (e.g., Leroy et al., 2011; Magdis et al., 2012; Schruba et al., 2012; Genzel et al.,

2012; Sandstrom et al., 2013) as well as theoretically (e.g., Wolfire et al. 2010, see also Bolatto et al. 2013).

We adopt the relation from Genzel et al. (2015, also adopted by Tacconi et al. 2018; Dessauges-Zavadsky et al. 2020),

$$\alpha_{\rm CO}(Z) = \alpha_{\rm CO}^{\rm MW} \times \sqrt{10^{-1.27(12+\log({\rm O/H})-8.67)}} \tag{6.3}$$

$$\times \sqrt{0.67 \exp\left(0.36 \times 10^{-(12+\log({\rm O/H})-8.67)}\right)}, \tag{6.4}$$

which is the geometrical mean of the curves from Genzel et al. (2012, which follows a power-law, as the other literature relations do) and Bolatto et al. (2013, which has a steeper, exponential increase towards very low metallicities). Here, $12 + \log({\rm O/H})$ is the gas-phase oxygen abundance, measured on the Pettini & Pagel (2004) scale (for conversion between metallicity scales see Kewley & Ellison 2008), calibrated to a solar abundance of $12 + \log({\rm O/H})_\odot = 8.67$ (Asplund et al., 2009), and $\alpha_{\rm CO}^{\rm MW} = 4.36\,{\rm M}_\odot({\rm K\,km\,s^{-1}\,pc^2})^{-1}$, which includes a factor 1.36 for helium (Strong & Mattox, 1996).

To obtain metallicities in the absence of a direct tracer, the mass metallicity relation can be used (see § 6.4.2 for discussion). Genzel et al. (2015) determined the following mass-metallicity relation.

$$12 + \log({\rm O/H})_{\rm PP04} = a - 0.087\left(\log M_* - b(z)\right)^2, \tag{6.5}$$

where $a = 8.74(0.06)$ and $b(z) = 10.4\,(0.05) + 4.46\,(0.3)\log(1+z) - 1.78\,(0.4)\log^2(1+z)$ (uncertainties in brackets), which is determined by combining several relations at different redshifts (Erb et al., 2006; Maiolino et al., 2008; Zahid et al., 2014; Wuyts et al., 2014). Notably, this relation approaches that of Maiolino et al. (2008) determined at $z = 3.5$.

Alternatively, we can determine $M_{\rm mol}$ from [C I], under the assumption of an excitation temperature $T_{\rm ex}$ and a neutral atomic carbon abundance (Weiß et al. 2005; see Boogaard et al. 2020 for a detailed description). We adopt $T_{\rm ex} = 30$ K (Walter et al., 2011, note that the atomic carbon mass is not a strong function of excitation temperature above $T_{\rm ex} = 20$ K) and an abundance of $[{\rm C\,I}]/[{\rm H_2}] = 2 \times 10^{-5}$ (Valentino et al., 2018; Boogaard et al., 2020). We will revisit the latter assumption in § 6.4.2.

The dust can be used as a third tracer of the molecular gas mass. We compute the dust mass by relying on assumption that the Rayleigh-Jeans (RJ) tail of the dust blackbody at long wavelengths is nearly always optically thin (Scoville et al., 2016). Specifically, we follow Magnelli et al. (2020) and assume a mass-weighted mean dust temperature of $\langle T_{\rm dust}\rangle_{\rm M} = 25$ K and a dust emissivity spectral index of $\beta = 1.8$. As argued by Scoville et al. (2016), the cold dust is the dominant contributor to the dust mass and the RJ-tail of the dust emission, and recent studies by *Planck* and *Herschel* have found the temperature to be in the range of 15–35 K (e.g., Abergel et al., 2011; Magnelli et al., 2014). Varying beta between $1.5 - 2.0$ (the range typically assumed for the larger grains that dominate the far-infrared emission, e.g., Da Cunha et al. 2008) impacts the dust masses by 20–40%. Varying the dust temperature between 15–35 K has a more significant impact on the inferred gas masses, ranging from a factor 5.0 to 0.5, because the observations at rest-frame 275 μm start probing the emission away from the RJ-tail and closer to the peak (this is further discussed in § 6.4.2). We correct for the impact

of the Cosmic Microwave Background on the equilibrium dust temperature and observed flux density (da Cunha et al., 2013), which increases the inferred mass by 10%.

To convert the dust masses to gas masses, we assume a metallicity dependent gas-to-dust ratio ($\delta_{\rm GDR} \simeq M_{\rm mol}/M_{\rm dust}$), with $\delta_{\rm GDR}(\rm Z_\odot) = 100$ (Draine et al., 2007), making the common assumption that the gas in our galaxies at $z = 3.45$ is predominately molecular (e.g., Daddi et al., 2010b; Genzel et al., 2015; Tacconi et al., 2018). The $\delta_{\rm GDR} \propto Z^\gamma$ has been observed to decrease close to linearly towards sub-solar metallicities (with $\gamma \approx -1$, e.g., Leroy et al., 2011; Magdis et al., 2012; Sandstrom et al., 2013; Saintonge et al., 2013). However, there is increasing evidence of a steeper relation for metallicities below $12 + \log(\rm O/H) \approx 8.0 - 8.1$; Rémy-Ruyer et al. (2014) find $\gamma \approx -3.1$ in local galaxies, while observations at $z \sim 2$ suggest that $\gamma < -2.2$ (Coogan et al., 2019), in agreement with the fiducial model from Popping et al. (2017a). We explore both regimes, assuming the power-law $\delta_{\rm GDR}(Z)$ relation from Tacconi et al. (2018) for a shallower increase with metallicity. For a steeper $\delta_{\rm GDR}(Z)$ at low metallicity, we adopt the broken power law relation from Rémy-Ruyer et al. (2014, the $X_{\rm CO,Z}$-case), which we scale to the same assumptions ($12 + \log(\rm O/H)_\odot = 8.67$; $\delta_{\rm GDR}(\rm Z_\odot) = 100$):

$$\delta_{\rm GDR}(Z) = \begin{cases} 10^{2+\gamma_{\rm H}(x-8.67)} & \text{for } x > 8.1 \\ 10^{0.8+\gamma_{\rm L}(x-8.67)} & \text{for } x \leq 8.1, \end{cases} \tag{6.6}$$

with $x = 12 + \log(\rm O/H)$. Here $\gamma_{\rm H} = -1$ and $\gamma_{\rm L} = -3.1$ are the power law slopes at high and low metallicity, respectively. The relation from Tacconi et al. (2018) is obtained from Equation 6.6 by taking the $x > 8.1$ solution at all metallicities, with $\gamma_{\rm H} = -0.85$.

6.4.2 Low metallicity driving a high molecular gas mass-to-light ratio

We show the constraints on the molecular gas mass in the context of the gas-to-stellar mass-ratio ($\mu_{\rm gas} = M_{\rm mol}/M_*$) and the gas fraction ($f_{\rm gas} = M_{\rm mol}/(M_{\rm mol} + M_*)$), including a literature sample of CO observations at low and high redshift, in Figure 6.8. At the basis of the literature sample, we take the mass-selected sample of Sloan Digital Sky Survey galaxies at $z = 0$ from xCOLDGASS (Saintonge et al., 2017), together with the massive, main-sequence selected galaxies at $z = 0.5 - 2.5$ from the Plateau de Bure HIgh-z Blue Sequence Survey (PHIBSS1+2) from the Tacconi et al. (2018) compilation, and the galaxies from ASPECS at $z = 1.0 - 3.6$ (Aravena et al., 2019; Boogaard et al., 2019). We supplement these with studies that contain observations of CO in (strongly lensed) star-forming galaxies at $z \geq 3$ from Magdis et al. (2012, 2017, using the updated values from Tan et al. 2013), Dessauges-Zavadsky et al. (2015, 2017, which include two sources from Riechers et al. 2010), Gowardhan et al. (2019) and Cassata et al. (2020, based on the sources from Schinnerer et al. 2016). We convert the literature observations to the metallicity dependent $\alpha_{\rm CO}$ (Equation 6.4; using the mass metallicity relation when needed, Equation 6.5) and adopt $r_{21} = 0.77$ and $r_{31} = 0.55$ (± 0.1; to remain consistent with Tacconi et al. 2018), though we keep the excitation corrections as assumed by the authors in case these are better constrained through additional line measurements (Boogaard et al., 2020; Cassata et al., 2020).[49]

[49] For example, in the case of ASPECS, the measured $\langle r_{31} \rangle = 0.8$ (Riechers et al., 2020; Boogaard et al., 2020), implies a factor 1.5× higher gas masses than the average value from Tacconi et al. (2018). Note however that, as

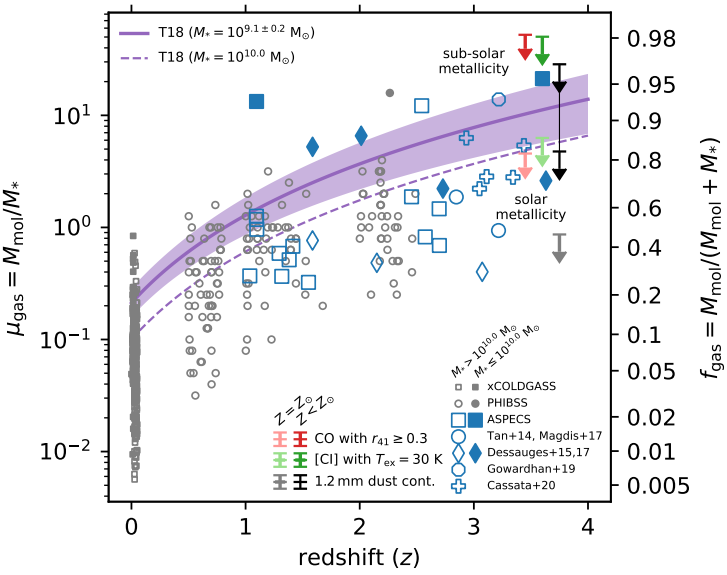

Figure 6.8: The gas-to-stellar mass ratio ($\mu_{\rm gas}$) and gas fraction ($f_{\rm gas}$) as a function of redshift. We show a literature sample of star-forming galaxies with CO measurements, focusing on $z \geq 3$, separating galaxies with $M_* \leq 10^{10}$ M$_\odot$ (filled symbols) and $M_* > 10^{10}$ M$_\odot$(open symbols). Nearly all galaxies from literature are significantly more massive than the $\langle z \rangle = 3.45$ star forming galaxies studied here, which have a median $M_* = 10^{9.1}$ M$_\odot$ and SFR $= 10\,{\rm M_\odot\,yr^{-1}}$. The upper limit on the gas fraction from CO is shown in red, with the limits at low and high gas fraction corresponding to solar metallicity ($\alpha_{\rm CO}^{\rm MW} = 4.36$; light red) and sub-solar metallicity ($\alpha_{\rm CO} = 50$; dark red), respectively, assuming $r_{41} \geq 0.3$. The green limit shows the constraints from [C I], for a typical abundance of 2×10^{-5} and a factor 8× lower in lighter and darker shading, respectively. The gray and black limits show the constraint from the 1.2 mm dust continuum assuming, in order of increasing gas fraction, $\delta_{\rm GDR} = 100$, 550 and 3300, corresponding to solar metallicity and sub-solar metallicity with different assumptions for the scaling of $\delta_{\rm GDR} \propto Z^\gamma$. We add horizontal offsets to the upper limits from different tracers for clarity. For comparison, we also show the predictions from Tacconi et al. (2018) for main-sequence galaxies with stellar masses $M_* = 10^{9.1\pm0.2}$ M$_\odot$ (solid line with shading; 0.2 dex around the median mass of our sample, where shading also includes the uncertainties in the fit of the scaling relation), and $10^{10.0}$ M$_\odot$ (dashed; above the most massive galaxy in our sample). Under the assumption of solar metallicity conversion factors, the constraints are in tension with the scaling relations from Tacconi et al. (2018) for galaxies in our mass range, while for sub-solar metallicity conversion factors the upper limits are in comfortable agreement.

argued in § 6.4.1, differences in the excitation do not affect the upper limit on the gas mass of our star-forming galaxies at $\langle z \rangle = 3.45$, unless the excitation is significantly lower than our (conservative) lower limit.

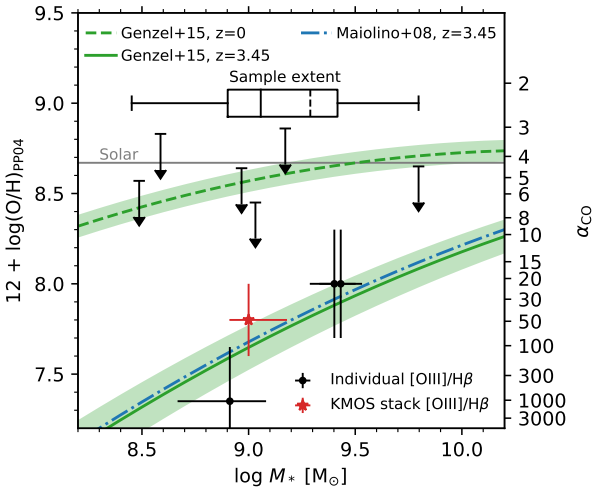

Figure 6.9: Plot of the mass–metallicity (MZ) relation and corresponding $\alpha_{\rm CO}(Z)$ (Equations 6.4 and 6.5; Genzel et al. 2015), as function of stellar mass (M_*). The constraints on the MZ relation at $z = 3.45$ come from Maiolino et al. (2008). Metallicity is plotted as 12 + log (O/H) on the Pettini & Pagel (2004) scale. The inset shows a boxplot with the whiskers indicating the full stellar mass extent of the sample, the box the interquartile range, the solid line the median, and the dashed line the (linear) mean M_* of the sample. The black points show direct constraints (3σ limits) on the metallicity of a few galaxies via [O III] λ5008/Hβ λ4863, with 0.3 dex uncertainty, using the direct method (Curti et al., 2017), conservatively assuming the upper branch solution for the upper limits. The red star shows the average metallicity from the stack of the KMOS spectra (Figure 6.10) at the mean stellar mass (error bars correspond to the 16th and 84th percentile). Overall, the measurements are consistent with the MZ relation at the typical redshift of the sample.

Assuming conversion factors that apply at solar metallicity ($\alpha_{\rm CO}^{\rm MW} = 4.36$, $\delta_{\rm GDR} = 100$), the stacking results imply gas fractions that appear to be in tension with the observed gas fractions in galaxies at $z \geq 3$ at a similar stellar mass (see Figure 6.8). This is in particular true for stringent limit based the dust, which places our low-mass galaxies among the lowest gas fractions observed at $z = 3 - 4$, with $f_{\rm gas} \leq 0.5$. For CO, the tension becomes more clear once we take into account that our galaxies are over an order of magnitude lower in stellar mass than the typical galaxy studied in molecular gas at high redshift. The gas fraction in star-forming galaxies is observed to increase towards lower masses and expected to be substantial for low-mass galaxies at these epochs (Scoville et al., 2016; Tacconi et al., 2018; Liu et al., 2019). For reference, we plot the predicted gas fraction for a main sequence galaxy with $M_* = 10^{9.1\pm0.2}$ M$_\odot$ from Tacconi et al. (2018),[50] taking into account an extra 0.2 dex uncertainty in the average stellar mass, as well as for $M_* = 10^{10}$ M$_\odot$ (that is, more massive than the most massive galaxy in our sample). Taking into account the evolution of

[50] We adopt the "$\beta = 0$" scaling relation from Tacconi et al. (2018), assuming a main sequence as observed by Whitaker et al. 2014.

the gas fraction in low-mass galaxies, the upper limit based on the CO is also tension with the expected gas fraction.

At face value, this result suggests that the galaxies in our sample have unexpectedly low molecular gas fractions. However, a more likely explanation is that the assumption of a Galactic $\alpha_{\rm CO}$ and gas-to-dust ratio does not hold for these systems. Indeed, significantly higher conversion factors would be naturally explained by sub-solar metallicities for these systems.

In Figure 6.9, we show the MZ relation from Equation 6.5 at the average redshift of our sample. We find that the metallicity at the median mass (16th, 84th percentile) of the sample is $12 + \log({\rm O/H}) = 7.7^{+0.3}_{-0.2}$. However, the MZ relation is only an approximate tracer of the metallicity. More directly, the [O III] λ5008/Hβ λ4863-ratio can be used to trace the metallicity, albeit with significant scatter, as the ratio monotonically increases with decreasing metallicity, up to a turnover at $12 + \log({\rm O/H}) \sim 8.0$ (e.g., Curti et al., 2017; Sanders et al., 2020). Because of this turnover, there are two metallicities solutions at a fixed ratio; one on the upper branch (high metallicity) and one on the lower branch (low metallicity). We robustly detect Hβ in two objects, finding high ratios of $\log([{\rm O\,III}]/{\rm H}\beta) \approx 0.8$ for two (MUSE-1019 and MUSE-6878). This roughly implies a metallicity at the turnover, $12 + \log({\rm O/H}) \sim 8.0$, via the direct method (Curti et al., 2017).[51] We also tentatively detect Hβ λ4863 in a third object (MUSE-6895), yielding a lower ratio (0.35), which implies a high metallicity if it is on the upper branch of the metallicity calibration, in tension with its stellar mass. However, assuming that it follows the (extrapolated) lower branch, this would imply a much lower metallicity of $12 + \log({\rm O/H}) \sim 7.35$ (and an extremely high $\alpha_{\rm CO} \gg 100$), in better agreement with the stellar mass. For the remaining galaxies, we only find (weak) upper limits on the metallicity (conservatively assuming all are on the higher branch).

To obtain an estimate of the average metallicity in the sample, we stack the KMOS spectra using weighted mean and median stacking. Because of the uncertainties in the background level (see § 6.2.2), we do not normalize the spectra but stack the continuum subtracted spectra instead, which may introduce a bias towards the brighter objects that go into the stack. Note that, due to the shifting to a common redshift, the skyline residuals are spread throughout the stack, though this problem should be mitigated in the median stack. The stacked spectra are shown in Figure 6.10. We tentatively detect Hβ λ4863, measuring $\log([{\rm O\,III}]/{\rm H}\beta) \approx 0.9 \pm 0.3$, which broadly implies a metallicity of $12 + \log({\rm O/H}) \approx 7.6 - 8.0$. We do caution against over-interpreting the stack, given the uncertainties mentioned above. It should also be stressed that the mass-metallicity relation only holds on average. For example, Dessauges-Zavadsky et al. (2017), found that the lensed arc at $z = 3.6$ has a higher inferred metallicity from its measured [O III]/Hβ-ratio than predicted from the MZ. Overall though, the metallicities for the individual galaxies and from the stack are in reasonable agreement with the predictions from the MZ relation (Figure 6.9), pointing to an average metallicity of $12 + \log({\rm O/H}) \approx 7.8 \pm 0.2$ for the galaxies in our sample.

The average metallicity of our sample implies a significantly higher value of $\alpha_{\rm CO} \approx 50$, which places our upper limit in comfortable agreement with the predicted gas fractions (see Figure 6.8). Notice that the strong, non-linear increase in the conversion factor with

[51] http://www.arcetri.astro.it/metallicity/calibrazioni.pl

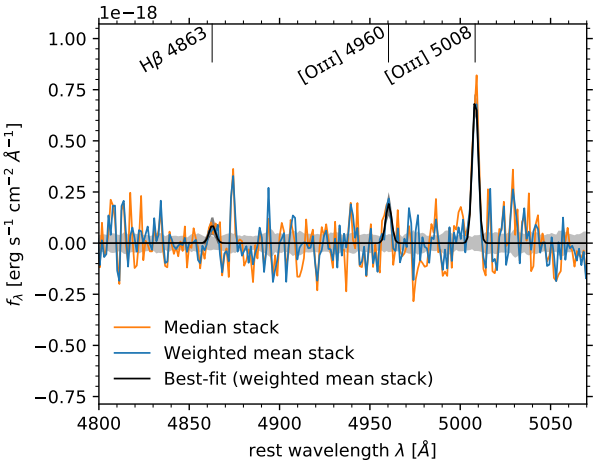

Figure 6.10: Stacked NIR spectra of the galaxies observed with KMOS (continuum subtracted). We show the median stack (orange), the weighted mean stack (blue, with propagated errors in gray) and the best-fit to the weighted mean stack (in black, with uncertainties). We tentatively detect Hβ λ4863, measuring $\log([\mathrm{O\,III}]/\mathrm{H}\beta) \approx 0.9 \pm 0.3$, which broadly implies a metallicity of $12 + \log(\mathrm{O/H}) \approx 7.6 - 8.0$ (Curti et al., 2017).

metallicity (Equation 6.4) makes the exact value uncertain, particularly in the low-mass range. Furthermore, we caution that there is still debate about the exact relation between α_{CO} and metallicity at low metallicity, mostly due to the difficulty of constraining α_{CO} at low metallicity. In any case, a minimal value of $\alpha_{\mathrm{CO}} \geq 10$ is required to place the 3σ upper limit on the Tacconi et al. (2018) relation, more than 2 times the Galactic value.

The shallower relations between gas-to-dust ratio and metallicity yield gas-to-dust ratios that are insufficient to reconcile the observed limit with the scaling relations, which requires a $\delta_{\mathrm{GDR}} \geq 1200$. For example, we find $\delta_{\mathrm{GDR}} \approx 550$ based on (Tacconi et al., 2018, see Equation 6.6). This points towards a steeper relation between the δ_{GDR} and metallicity in the low-metallicity regime, as suggested by, for example, Rémy-Ruyer et al. (2014) and Coogan et al. (2019) (see § 6.4.1). Adopting the relation from Rémy-Ruyer et al. (2014, Equation 6.6) yields a significantly higher $\delta_{\mathrm{GDR}} \approx 3300$, again placing our upper limit in comfortable agreement with the expected gas fraction. Alternatively, a dust temperature of $T_{\mathrm{dust}} < 20$ K (as opposed to 25 K), can also reconcile the difference with a lower δ_{GDR}. However, given the stronger radiation field expected at low metallicity, it is not clear that the dust temperatures would be much lower than assumed.

Independent of CO and the dust, we reach the same conclusions using [C I] instead. While a typical abundance ratio of 2×10^{-5} predicts similarly low gas masses as CO, assuming an 8× lower abundance (loosely based on the metallicity) easily yields a limit that is fully consistent with the scaling relations, with a $\approx 2\times$ lower abundance being minimally required (see Figure 6.8).

6.4.3 Contribution to the cosmic molecular gas density

The galaxies under study are below the detection threshold of current $\rho_{\rm mol}(z)$ surveys (e.g., Riechers et al., 2019; Decarli et al., 2019, 2020). Still, their potentially high gas mass-to-light ratios imply that they could have a significant contribution to the total cosmic molecular gas density. Assuming the average gas masses derived from the stacks are representative of all 67 galaxies in the photometric catalog down to $H_{\rm F160W} = 26$ (cf. Figure 6.1), we compute the total contribution of these galaxies to the cosmic molecular gas density, $\rho(3.0115 < z < 3.812)$. We adopt the solar, the minimum, and the sub-solar conversion factors from § 6.4.2, and $r_{41} = 0.5$. The result can be seen in Figure 6.11. Because the upper limits are not stringent enough, the results are inconclusive. On one hand, they do not exclude the possibility that a significant amount of molecular gas is missed due to the high gas mass-to-light ratio of star forming galaxies at these redshifts. On the other hand, it is equally possible that their contribution is significantly smaller, implying that their molecular gas signal lies well below the detection threshold, even in stacks. We also determine upper limits for the more massive galaxies in the sample only (with $M_* \geq 10^9$ M$_\odot$ and $\geq 10^{9.5}$ M$_\odot$, computing their average conversion factors from the mass-metallicity relation). The limits on $\rho_{\rm mol}$ are slightly stronger for these sub-samples because, while the stacks are slightly less constraining, the estimated $\alpha_{\rm CO}$ and $\delta_{\rm GDR}$ are lower, as well as the number of sources in the volume. The results fall in between the minimum and sub-solar values of magnitude limited sample, but do not alter the conclusions overall.

6.4.4 Implications for observing cold gas in low metallicity galaxies at high redshift

The evolution of the metallicity of star-forming galaxies with redshift has significant implications for the detectability of molecular gas at $z \geq 3$. Even in the local universe, detecting CO in low metallicity dwarf galaxies has been challenging (e.g., Schruba et al., 2012; Hunt et al., 2015). The substantial CO-to-H_2 conversion factor and gas-to-dust ratios inferred for our low-mass, low metallicity galaxies imply that detecting the molecular gas reservoir in these galaxies will be very challenging on an individual basis, even with modern instruments. Similar conclusions are also reached for more massive galaxies at sub-solar metallicities (e.g. Tan et al., 2013; Coogan et al., 2019). Tan et al. (2013) have shown that under the assumption of a MZ-$\alpha_{\rm CO}$ relation similar to the one adopted here, the expected CO luminosity for a star-forming galaxy on the main sequence rapidly declines, due to the metallicity evolution. This raises the interesting question of how the molecular gas content can be best constrained in sub-solar metallicity star-forming galaxies at high redshift.

There are significant uncertainties in deriving a total dust and gas mass from the dust continuum in the low metallicity regime. Variations in the process and balance of dust formation and destruction at low metallicity, as well as differences in grain composition and size distribution can have a major impact on the gas-to-dust ratio, the dust emissivity and emerging dust spectrum (e.g., Rémy-Ruyer et al. 2014, see also Draine et al. 2007). In addition to these complications, the fainter part Rayleigh-Jeans tail at long wavelengths has to be probed, such that the blackbody is dominated by cold dust which dominates the mass

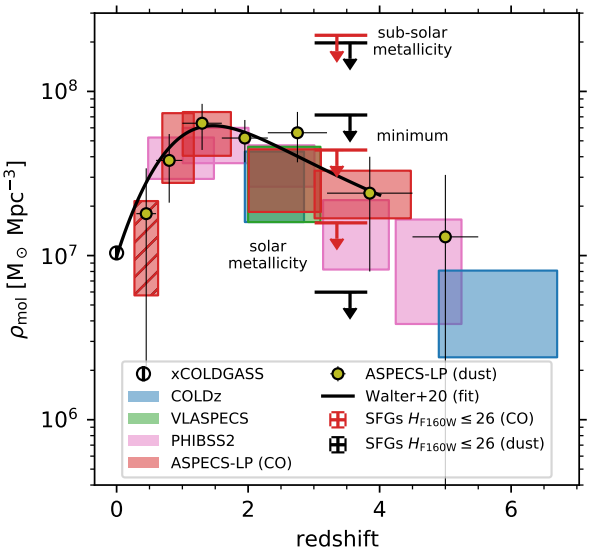

Figure 6.11: Cosmic molecular gas density as a function of redshift. The literature data is from Fletcher et al. (2020) (xCOLDGASS), Riechers et al. (2019) (COLDz), Riechers et al. (2020) (VLASPECS), Lenkić et al. (2020) (PHIBSS2), Decarli et al. (2020) (ASPECS-LP CO), Magnelli et al. (2020) (ASPECS-LP dust) and we also show the best-fit from Walter et al. (2020). We show the best-estimate upper limit on the cosmic molecular density for all galaxies with $H_{F160W} \leq 26$ at $3.0115 < z < 3.812$, as derived from CO (red; assuming $r_{41} = 0.5$) and the dust-continuum (black). The different limits are for conversion factors (α_{CO}, δ_{GDR}) = (3.6, 100), (10, 1200), (50, 3300), corresponding to solar metallicity, the minimum value based on § 6.4.2, and the best-estimate sub-solar metallicity. The upper limits do not rule out a large amount of molecular gas in lower mass galaxies (that would have been missed in previous surveys, due to their high gas mass-to-light ratio), but are equally consistent with a smaller contribution to the total molecular gas budget.

and the uncertainty in the (unknown) mass-weighted dust-temperature is minimized (e.g. Scoville et al., 2016).

At low metallicity, CO also becomes an increasingly poor tracer of the total molecular gas reservoir. Because of the lower dust abundance at low metallicity, CO is dissociated and ionized into C and C^+ deeper into the clouds, while the H_2 self-shields against photodissociation (Gnedin & Draine, 2014), resulting in an increasing volume of H_2 gas that is not traced by CO at low metallicity (e.g., Wolfire et al., 2010). This provides motivation to investigate and develop the theoretical underpinning for other species as tracers of the molecular gas, such as the fainter [C I] lines (e.g., Weiß et al. 2003, 2005; Papadopoulos et al. 2004; see also Valentino et al. 2018; Boogaard et al. 2020), but in particular also [C II] $\lambda 158\,\mu$m.

The bright [C II] $^3P_{3/2} \rightarrow {}^3P_{1/2}$ line at 158 μm is one of the foremost cooling lines of the ISM, also at low metallicity (where it is outranked only by the high ionization line [O III] $\lambda 88\,\mu$m at 35 eV; e.g., Cormier et al., 2015, 2019) and its high luminosity allows it

to be observed in star-forming galaxies out to the highest redshifts (Ouchi et al., 2013; Ota et al., 2014; Maiolino et al., 2015; Capak et al., 2015; Knudsen et al., 2016; Pentericci et al., 2016; Bradač et al., 2017; Matthee et al., 2017, 2019; Carniani et al., 2018a,b, 2020; Smit et al., 2018; Hashimoto et al., 2018; Laporte et al., 2019; Le Fèvre et al., 2020; Béthermin et al., 2020; Harikane et al., 2020; Bakx et al., 2020). With an ionization potential of 11.3 eV (that is, lower than H I at 13.6 eV), [C II] can arise in both the neutral and ionized medium, though it becomes an increasingly better tracer of the neutral ISM towards lower metallicities (Croxall et al. 2017; Cormier et al. 2019, see also Díaz-Santos et al. 2017) potentially due to the carbon in the H II-regions being further ionized into C^{++} (as witnessed by the shift in the ionization balance to high ionization lines, also see in some high-z sources, e.g., Pavesi et al. 2016; Harikane et al. 2020, see also Carniani et al. 2020). While, as a cooling line, [C II] is in principal sensitive to the heating rate (and not the molecular gas mass), it may be calibrated as a molecular gas tracer (Zanella et al., 2018). As such, [C II] can potentially outperform other tracers of the molecular gas mass, in particular in low metallicity environments (e.g. Madden et al., 2020). As [C II] is already seeing use as tracer of the molecular gas at high redshift (e.g., Dessauges-Zavadsky et al., 2020), its use to this end should be further investigated both observationally and theoretically.

6.5 Summary and conclusions

We present constraints on the molecular gas signal for a sample of 24 star-forming galaxies at $\langle z \rangle = 3.45$, with a median $M_* = 10^{9.1}\,M_\odot$, in the *Hubble* Ultra Deep Field (HUDF). Based on their Lyα- and H_{F160W}-selection (Figure 6.1), they show relatively low $EW^0_{Ly\alpha} \approx 20$ Å ($L_{Ly\alpha} = 0.2\,L^*_{Ly\alpha}$), and rest-frame UV spectra similar to star-forming galaxies at the same epoch (see Figure 6.4). We efficiently follow-up Lyα-selected galaxies from the MUSE HUDF Survey, with near-infrared spectroscopy from KMOS and MOSFIRE to determine their systemic redshifts (Figure 6.2 and Figure 6.12) and stack the molecular line emission from the ALMA Spectroscopic Survey in the HUDF (ASPECS). Our main results are as follows:

- We determine systemic redshifts from the rest-frame UV and rest-frame optical features, finding an average velocity offset of $\langle \Delta v(Ly\alpha) \rangle = 346$ km s^{-1} (with a 100 to 600 km s^{-1} range) consistent with the relatively low $EW^0_{Ly\alpha}$ of the sample (Figure 6.5).

- Stacking the signal from ^{12}CO $J = 4 \rightarrow 3$ and [C I] $^3P_1 \rightarrow {}^3P_0$ (as well as the ^{12}CO $J = 9 \rightarrow 8$ and $J = 10 \rightarrow 9$ lines), we do not find any detections and determine 3σ upper limits on the line luminosities of 4.0×10^8 K km s^{-1}pc^2 and 5.6×10^8 K km s^{-1}pc^2, respectively, for a linewidth of 300 km s^{-1} (see Figure 6.6 and Table 6.1; also for the limits on the higher-J lines). Stacking the 1.2 mm dust continuum, we find a 3σ upper limit on the flux density of $S_\nu \leq 9\,\mu$Jy (Figure 6.7).

- Comparing the inferred molecular fraction from CO and the dust continuum to scaling relations, we find that assuming a 'Galactic' $\alpha^{MW}_{CO} = 4.36$ and $\delta_{GDR} = 100$ significantly underpredicts the expected molecular gas mass (Figure 6.8). In order to reconcile our measurements with the published scaling relations from Tacconi et al. (2018) would

require an $\alpha_{\rm CO} \geq 10$ and $\delta_{\rm GDR} \geq 1200$. This result either implies that our galaxies have unexpectedly low gas fractions or that the assumption of solar-metallicity conversion factors break down.

- Using the mass-metallicity relation, as well as constraints from [O III] λ5008/Hβ λ4863 (Figure 6.10), we predict an average metallicity of our sample of $12 + \log({\rm O/H}) = 7.8 \pm 0.2$, that is, significantly sub-solar. This implies a high $\alpha_{\rm CO} \approx 50$ making our result consistent with the expected (high) gas fractions at $z = 3.5$ (Figure 6.9).

- An approximately linear scaling relation between the gas-to-dust ratio and metallicity ($\delta_{\rm GDR} \propto \gamma^{-0.85}$; Tacconi et al., 2018) yields $\delta_{\rm GDR} \approx 550$, which is insufficient to reconcile the limit based on the dust with the Tacconi et al. (2018) scaling relations. Using a steeper relation at low metallicity ($\delta_{\rm GDR} \propto \gamma^{-3.1}$ at $12 + \log({\rm O/H}) \leq 8.1$; Rémy-Ruyer et al., 2014) instead yields $\delta_{\rm GDR} \approx 3300$, making our upper limit consistent again (Figure 6.8).

- Independent of the CO, we find the same tension from the [C I] luminosity, which implies a [C I]/[H_2] abundance lower than in massive star-forming galaxies such as the Milky Way (Figure 6.8).

- Based on the results, we compute the upper limit on the contribution of all galaxies with $H_{\rm F160W} \leq 26$ to the cosmic molecular gas density $\rho_{\rm mol}(z = 3.0115 - 3.812)$. The upper limits are not constraining enough to exclude the possibility of a significant contribution of these galaxies, that lie below the detection threshold of current surveys, to the cosmic molecular gas density.

The results of this work exemplify the difficulty to obtain molecular gas mass estimates in low metallicity environments, which are expected to be more prevalent in typical star forming galaxies at $z \geq 3$. Given the uncertainties associated with the dust and CO at low metallicity we argue for the further observational and theoretical development of alternative tracers of the molecular gas reservoir, such as the bright [C II] λ158 μm line, that should be more easily observable with ALMA. Obtaining accurate constraints on the gas-phase metallicity of high-redshift galaxies will key in this regard and one of the key pieces of information that the *James Webb Space Telescope* will be able to provide.

Acknowledgments

L.A.B. is grateful to Corentin Schreiber for assisting with the near-infrared spectroscopy during the early stages of this work. L.A.B. acknowledges support from the Leids Kerkhoven-Bosscha Fonds under subsidy numbers 18.2.074 and 19.1.147. D.R. acknowledges support from the National Science Foundation under grant numbers AST-1614213 and AST-1910107. D.R. also acknowledges support from the Alexander von Humboldt Foundation through a Humboldt Research Fellowship for Experienced Researchers. A.F. acknowledges the support from grant PRIN MIUR 2017-20173ML3WW_001. J.B. acknowledges support by Fundação para a Ciência e a Tecnologia (FCT) through the research grants UID/FIS/04434/2019,

UIDB/04434/2020, UIDP/04434/2020. H.I. acknowledges support from JSPS KAKENHI Grant Number JP19K23462. This work is based on observations collected at the European Southern Observatory under ESO programs 094.A-2089(B), 095.A-0010(A), 096.A-0045(A), 096.A-0045(B), 099.A-0858(A), and 0101.A-0725(A). This paper makes use of the following ALMA data: ADS/JAO.ALMA#2016.1.00324.L. ALMA is a partnership of ESO (representing its member states), NSF (USA) and NINS (Japan), together with NRC (Canada), NSC and ASIAA (Taiwan), and KASI (Republic of Korea), in cooperation with the Republic of Chile. The Joint ALMA Observatory is operated by ESO, AUI/NRAO and NAOJ. The National Radio Astronomy Observatory is a facility of the National Science Foundation operated under cooperative agreement by Associated Universities, Inc. This work was supported by a NASA Keck PI Data Award, administered by the NASA Exoplanet Science Institute. Data presented herein were obtained at the W. M. Keck Observatory from telescope time allocated to the National Aeronautics and Space Administration through the agency's scientific partnership with the California Institute of Technology and the University of California. The Observatory was made possible by the generous financial support of the W. M. Keck Foundation. The authors wish to recognize and acknowledge the very significant cultural role and reverence that the summit of Maunakea has always had within the indigenous Hawaiian community. We are most fortunate to have the opportunity to conduct observations from this mountain.

Facilities: ALMA, VLT: Yepun (MUSE), VLT: Antu (KMOS), Keck I (MOSFIRE). *Software:* TOPCAT (Taylor, 2005), GNUASTRO (Akhlaghi & Ichikawa, 2015), IPYTHON (Perez & Granger, 2007), NUMPY (van der Walt et al., 2011), MATPLOTLIB (Hunter, 2007), ASTROPY (The Astropy Collaboration et al., 2013, 2018), CASA (McMullin et al., 2007).

Appendix 6.A Table

The coordinates, (systemic) redshifts, and physical properties of the sample of $3.0115 < z < 3.812$ star-forming galaxies are listed in Table 6.2.

Table 6.2: Coordinates, (systemic) redshifts, and physical properties of the sample of $3.0115 < z < 3.812$ star-forming galaxies.

ID	RAF ID	α_{J2000}	δ_{J2000}	$z^{\rm red}_{\rm Lyff}$	$\delta(z^{\rm red}_{\rm Lyff})$ ($\rm km\,s^{-1}$)	$z_{\rm sys}$	$\delta(z_{\rm sys})$ ($\rm km\,s^{-1}$)	Source	$\Delta v(\rm Ly\alpha)$ ($\rm km\,s^{-1}$)	$\log M_*$ ($\rm M_\odot$)	log SFR ($\rm M_\odot\,yr^{-1}$)
(1)	(2)	(3)	(4)	(5)	(6)	(7)	(8)	(9)	(10)	(11)	(12)
50	9110	53.16284897	-27.77162645	3.33015 ± 0.00086	59.5	3.32349 ± 0.00027	18.7	MUSE EM	461.8 ± 62.5	$9.15^{+0.10}_{-0.12}$	$1.122^{+0.10}_{-0.10}$
82	6627	53.1515512	-27.7853475	3.60777 ± 0.00006	3.9	3.60493 ± 0.00080	52.1	MUSE EM	184.9 ± 52.3	$9.00^{+0.10}_{-0.10}$	$0.792^{+0.10}_{-0.17}$
106	9863	53.16372638	-27.77907551	3.28171 ± 0.00009	6.3	3.27648 ± 0.00012	8.4	MUSE EM	366.6 ± 10.5	$8.45^{+0.10}_{-0.10}$	$0.547^{+0.10}_{-0.10}$
118	23839	53.15708801	-27.78026883	3.02127 ± 0.00056	41.7	3.01727 ± 0.00017	12.7	MUSE EM	298.5 ± 43.7	$8.78^{+0.10}_{-0.20}$	$0.462^{+0.10}_{-0.10}$
1019	8002	53.16492565	-27.76512153	3.19361 ± 0.00088	62.9	3.18669 ± 0.00002	1.4	MOSFIRE	495.5 ± 63.0	$9.43^{+0.10}_{-0.10}$	$1.387^{+0.10}_{-0.10}$
...	...	...	...	...	...	3.18579 ± 0.00026	18.6	MUSE ABS	560.1 ± 65.7	...	...
1059	8203	53.15344247	-27.76611934	3.80588 ± 0.00005	3.1	3.80122 ± 0.00199	124.3	MUSE ABS	291.0 ± 124.4	$9.70^{+0.10}_{-0.10}$	$1.267^{+0.10}_{-0.10}$
1087	3506	53.16790037	-27.7979532	3.46259 ± 0.00019	12.8	3.45675 ± 0.00097	65.2	MUSE ABS	392.8 ± 66.6	$9.55^{+0.10}_{-0.10}$	$1.112^{+0.10}_{-0.10}$
1088	6012	53.15257181	-27.79384452	...	...	3.08224 ± 0.00039	28.6	MUSE ABS	...	$9.65^{+0.10}_{-0.10}$	$1.472^{+0.10}_{-0.10}$
1113	8528	53.16993928	-27.76833978	3.09022 ± 0.00005	3.7	3.08803 ± 0.00281	206.1	KMOS	160.6 ± 206.2	$9.17^{+0.17}_{-0.10}$	$0.917^{+0.10}_{-0.10}$
...	...	...	...	...	...	3.08520 ± 0.00065	47.7	MUSE ABS	368.4 ± 47.9	...	...
1138	8308	53.14850621	-27.77728375	3.61287 ± 0.00266	172.9	3.60520 ± 0.00047	30.6	MUSE ABS	499.3 ± 175.9	$9.40^{+0.11}_{-0.10}$	$1.567^{+0.10}_{-0.10}$
1215	9247	53.1487158	-27.77294489	3.33215 ± 0.00155	107.3	3.32623 ± 0.00104	72.1	KMOS	410.2 ± 129.4	$9.87^{+0.10}_{-0.10}$	$1.092^{+0.17}_{-0.10}$
...	...	...	...	...	...	3.32594 ± 0.00053	36.7	MUSE ABS	430.4 ± 113.5	...	...
1253	8783	53.17824938	-27.77399604	3.67218 ± 0.00096	61.6	3.66765 ± 0.00421	270.4	KMOS	291.0 ± 277.6	$8.59^{+0.10}_{-0.10}$	$0.587^{+0.10}_{-0.10}$
...	...	...	...	...	...	3.66896 ± 0.00067	43.0	MUSE EM	206.8 ± 75.2	...	...
1360	37765	53.17926551	-27.78289487	3.66696 ± 0.00161	103.4	3.66479 ± 0.00284	182.5	MUSE ABS	139.5 ± 209.9	$9.06^{+0.12}_{-0.10}$	$1.027^{+0.10}_{-0.28}$
1530	7002	53.17666134	-27.78380467	3.19270 ± 0.00112	80.1	3.18896 ± 0.00036	25.8	KMOS	267.7 ± 84.2	$8.97^{+0.10}_{-0.10}$	$0.772^{+0.10}_{-0.10}$
1833	3673	53.1524905	-27.79770827	3.01437 ± 0.00178	132.9	3.00842 ± 0.00009	6.7	MOSFIRE	445.0 ± 133.3	$8.49^{+0.14}_{-0.10}$	$0.362^{+0.10}_{-0.36}$
6375	22525	53.14339467	-27.78800227	3.41682 ± 0.00160	108.6	3.41287 ± 0.01914	1300.3	KMOS	268.3 ± 1306.0	$8.79^{+0.10}_{-0.10}$	$0.882^{+0.10}_{-0.10}$
6518†	52206	53.14325211	-27.7868279	3.75265 ± 0.00062	39.1	3.74969 ± 0.00020	12.6	MOSFIRE	186.8 ± 41.1	...	...
6666	24954	53.15957552	-27.7767193	3.43869 ± 0.00021	14.2	3.43494 ± 0.00024	16.2	KMOS	253.5 ± 21.6	$9.03^{+0.10}_{-0.10}$	$0.902^{+0.10}_{-0.12}$
...	...	...	...	...	...	3.43492 ± 0.00008	5.4	MUSE EM	254.8 ± 15.2	...	...
6878	7843	53.13953672	-27.78067557	3.60787 ± 0.00090	58.6	3.60020 ± 0.00064	41.7	MUSE ABS	499.8 ± 72.0	$9.40^{+0.10}_{-0.11}$	$1.387^{+0.10}_{-0.13}$
...	...	...	...	...	...	3.60295 ± 0.00006	3.9	MOSFIRE	320.4 ± 58.7	...	...
6883	9832	53.17629722	-27.77891257	3.19503 ± 0.00222	158.6	3.18724 ± 0.00040	28.6	MUSE ABS	557.7 ± 161.5	$9.56^{+0.10}_{-0.10}$	$1.407^{+0.10}_{-0.10}$

Table 6.2: *(continued)*

ID	RAF ID	α_{J2000}	δ_{J2000}	$z_{\rm Lyff}^{\rm red}$	$\delta(z_{\rm Lyff}^{\rm red})$ ($\rm km\,s^{-1}$)	$z_{\rm sys}$	$\delta(z_{\rm sys})$ ($\rm km\,s^{-1}$)	Source	$\Delta v(\rm Ly\alpha)$ ($\rm km\,s^{-1}$)	$\log M_*$ ($\rm M_\odot$)	log SFR ($\rm M_\odot\,yr^{-1}$)
(1)	(2)	(3)	(4)	(5)	(6)	(7)	(8)	(9)	(10)	(11)	(12)
6895	5742	53.1759691	-27.79261283	3.71273 ± 0.00194	123.4	3.70409 ± 0.00079	50.3	MUSE ABS	550.6 ± 133.5	$8.41^{+0.10}_{-0.10}$	$0.497^{+0.10}_{-0.10}$
...	...	...	...	...	...	3.70522 ± 0.00020	12.7	KMOS	478.5 ± 124.3	...	...
8041	8635	53.1755829	-27.76874786	...	...	3.69700 ± 0.00172	109.8	MUSE ABS	...	$9.52^{+0.10}_{-0.10}$	$1.317^{+0.10}_{-0.16}$
8091	5468	53.14920592	-27.79147296	...	...	3.55707 ± 0.00116	76.3	MUSE ABS	...	$9.27^{+0.10}_{-0.10}$	$1.242^{+0.10}_{-0.10}$
8103	5741	53.17592521	-27.79246095	...	...	3.70527 ± 0.00027	17.2	MUSE EM	...	$8.60^{+0.10}_{-0.10}$	$0.677^{+0.10}_{-0.16}$

Notes. (1) MUSE ID (2) Rafelski et al. (2015) ID (3) Right Ascension (4) Declination (5) Redshift measured from Lyα λ1216 (the red peak, in the case of a double-peaked line) (6) Velocity uncertainty on redshift (7) Systemic redshift (8) Velocity uncertainty on systemic redshift (9) Source of systemic redshift (MUSE EMission or ABSorption, KMOS, MOSFIRE) (10) Lyα velocity offset, $\Delta v(\rm Ly\alpha) = c(z_{\rm Lyff}^{\rm red} - z_{\rm sys})/(1 + z_{\rm sys})$. (11) Stellar mass and (12) Star Formation Rate from MAGPHYS, with a minimum uncertainty of 0.1 dex.

† Blended with a $z = 0.83$ foreground object.

Appendix 6.B Spectra

The rest-frame UV (MUSE) and near-IR (KMOS, MOSFIRE) spectra of all galaxies in the sample are shown in Figure 6.12 (except for the galaxy already shown in Figure 6.2).

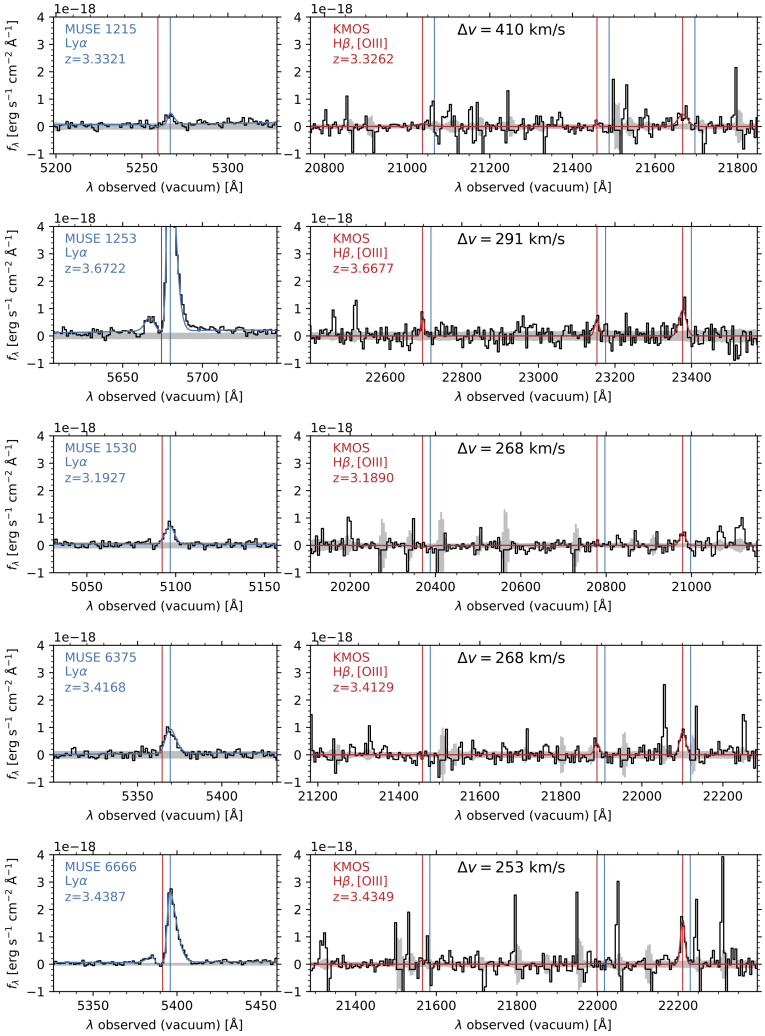

Figure 6.12: Rest-frame ultraviolet and optical spectra for the galaxies with near-infrared follow up. The *left* panel shows the MUSE spectrum surrounding the Lyα line. The *right* panel shows the continuum subtracted KMOS or MOSFIRE spectrum (indicated in the figure) around the Hβ λ4863 and [O III] $\lambda\lambda$4960, 5008 lines. In both panels the vertical blue and red lines indicate the redshift of Lyα and the systemic redshift, respectively, determined from the fit to the spectrum (shown in the same color). All spectra show a positive velocity offset between the red peak of Lyα and the systemic redshift.

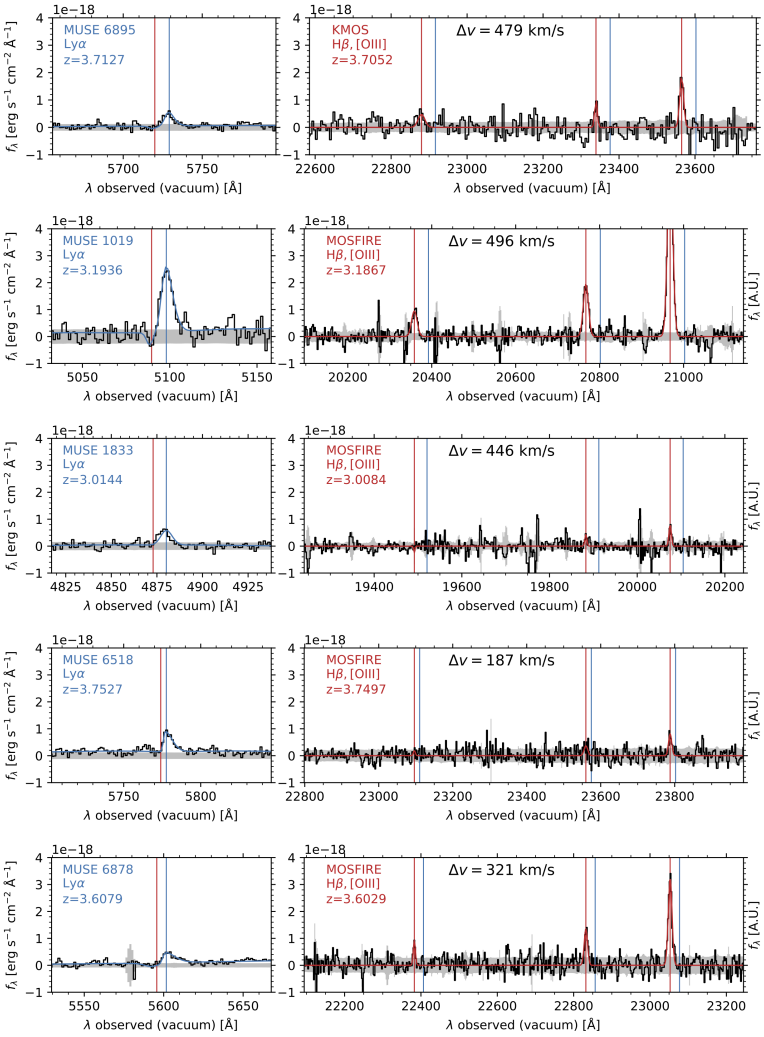

Figure 6.12: *(continued)*